Significant enhancement of the thermoelectric performance in $Ca_3Co_4O_9$ thermoelectric materials through combined strontium substitution and hot-pressing process

M. A. Torres,[1] F. M. Costa,[2] D. Flahaut,[3] K. Touati,[4] Sh. Rasekh,[2,5] N. M. Ferreira,[2,5] J. Allouche,[3] M. Depriester,[4] M. A. Madre,[1] A. V. Kovalevsky,[5] J. C. Diez,[1] A. Sotelo[1,*]

[1]ICMA (CSIC-Universidad de Zaragoza), C/María de Luna 3, 50018-Zaragoza (Spain).

[2]i3N, Departamento de Física, Universidade de Aveiro, 3810-193 Aveiro (Portugal).

[3]CNRS/Univ. Pau & Pays de l'Adour, Institut des Sciences Analytiques et de Physico-chimie pour l'Environnement et les Matériaux, UMR5254, 64000, Pau (France).

[4]UDSMM (EA 4476), MREI-1, Université du Littoral Côte d'Opale, 59140 Dunkerque (France).

[5]CICECO – Aveiro Institute of Materials, Department of Materials and Ceramic Engineering, University of Aveiro, 3810-193 Aveiro (Portugal).

Abstract

This work explores the possibilities for a further enhancement of the thermoelectric properties of $Ca_3Co_4O_9$ by Sr-doping combined with hot-pressing. Modified hot-pressing process resulted in highly-textured and dense ceramics. Sr-doping significantly improves electrical properties, resulting in extremely large power factor ($1.2mW/K^2m$ at 800ºC) due to simultaneous electrical resistivity decrease and Seebeck coefficient increase. The main effect on cumulative electrical performance is provided by the Seebeck coefficient, reaching 270µV/K at 800ºC. XPS revealed relatively high average cobalt oxidation state at room temperature (+3.3), compared to materials produced by

conventional sintering. The results of combined XPS and Auger electron spectroscopy emphasize the importance of high densification in $Ca_3Co_4O_9$-based ceramics for preventing phase decomposition and interaction with CO_2 and moisture. Still, despite the exceptional electrical performance, the calculated figure-of-merit (estimated as 0.29 at 800ºC) is around the best reported in the literature due to a high thermal conductivity (4.4W/K m at room temperature).

Keywords: Ceramics; Oxides; Hot-pressing; Texture; Electrical properties

Authors contribution: All authors have equally contributed to the article.

* Corresponding author: A. Sotelo (asotelo@unizar.es). ICMA (CSIC-Universidad de Zaragoza), C/María de Luna 3, 50018-Zaragoza (Spain). Tel.: +34 976762617

1. Introduction

Thermoelectric (TE) materials are characterized by their ability to directly convert heat into electrical energy due to the Seebeck coefficient (thermoelectric effect). The thermoelectric efficiency is generally determined by the temperature gradient and the dimensionless figure of merit, ZT; the latter quantity is related to the basic material properties, and is defined as $TS^2/\rho\kappa$, where S is Seebeck coefficient, ρ, electrical resistivity, κ, thermal conductivity, and T is the absolute temperature [1]. In the current climate change scenario, thermoelectricity has attracted much attention as a solution to improve the efficiency of the classical energy conversion systems by harvesting the waste heat [2]. As a consequence, the TE technology is expected to help fighting against climate change by decreasing the fossil fuels consumption and reducing the amount of released CO_2. On the other hand, thermoelectrics can be also used to produce renewable energy in solar thermoelectric generators [3], or in heating/refrigeration devices [4]. Nowadays, these commercial applications involve intermetallic thermoelectric materials, such as Bi_2Te_3 or $CoSb_3$, with high thermoelectric performances at relatively low temperatures [5,6]. However, they are known to degrade at moderately high temperatures under air atmosphere and/or release toxic or heavy elements. High operation temperatures are also favorable in terms of higher Carnot efficiency of the energy conversion. The first step to overcome high-temperature limitation of TE technology was done by the discovery of attractive thermoelectric properties in $Na_2Co_2O_4$ [7], showing that oxides can represent a suitable alternative to traditional thermoelectrics. As a consequence, cobalt oxide-based materials have been the focus of many works, especially on the $Ca_3Co_4O_9$ phase [8-10], since, besides

reasonable TE performance, they can operate at high temperatures in air without degradation.

The anisotropic behaviour of these materials [11] has been exploited to preferentially align their grains to enhance the electrical conductivity, aiming the properties of polycrystalline bulk materials similar to those of single crystals. On the other hand, the decrease of electrical resistivity is usually accompanied by the reduction of Seebeck coefficient and the increase in thermal conductivity values, as all three factors are linked to each other. Due to these characteristics, the improvement of ZT in these materials has been shown as a very difficult task. Consequently, several approaches have to be used simultaneously to maximize ZT values in $Ca_3Co_4O_9$ as, for example, texturing and doping. Among the texturing techniques, it is important to highlight the spark plasma sintering (SPS) [12,13], sinter-forging [14], template grain growth (TGG) [15], laser floating zone (LFZ) [16], and the electrically-assisted laser floating zone method (EALFZ) [17]. When considering doping processes, it should be distinguished between alio- and isovalent substitution, (i.e. Yb^{3+} for Ca^{2+}, and Sr^{2+} for Ca^{2+}, respectively) [18,19]. In the first situation, Yb decreases the rock-salt layer size (which should be reflected in a raise of electrical resistivity and Seebeck coefficient) and charge (decreasing the Co^{4+} proportion in the conduction layer, decreasing Seebeck coefficient and electrical conductivity). Moreover, its high atomic mass increases phonon scattering, leading to a lower thermal conductivity than the determined in undoped samples [20]. This is a very complex situation when compared with the effect of isovalent substitution, where only modifications in the rock-salt layer dimensions, and on the phonon scattering, are present.

4

This work aims at producing high-density textured undoped and Sr-doped $Ca_3Co_4O_9$ ceramic materials, with expected enhancement of the thermoelectric induced by doping and texturing processes. Based on previously published results [21-24], these samples were prepared through the classical solid state method, and textured using the hot-uniaxial pressing technique. The structural and microstructural features of these samples were studied and correlated with the thermoelectric properties.

2. Experimental

2.1. Samples preparation

The initial $Ca_3Co_4O_9$ and $Ca_{2.93}Sr_{0.07}Co_4O_9$ ceramic precursors used in this work were prepared from commercial $CaCO_3$ ($\geq$ 99 %, Aldrich), $SrCO_3$ ($\geq$ 98%, Aldrich), and CoO (99.99 %, Aldrich) powders using the classical solid state method. The powders were weighed in the adequate proportions, mixed, and ball milled in an agate ball mill at 300 rpm for 30 min in water medium. The resulting slurry was then dried under infrared radiation, followed by a two-step thermal treatment at 750 and 800 ºC for 12 h, under air atmosphere, with an intermediate manual milling. The thermal treatment was performed in order to assure total decomposition of carbonates, in agreement with previous works [25]. These pre-reacted powders were subsequently cold uniaxially pressed at around 300 MPa in the shape of disks (25 mm diameter and 5 mm thick) which were sintered at 900 ºC for 24 h, under air, with a final furnace cooling to form the $Ca_3Co_4O_9$ phase in the sintered samples. Finally, the sintered disks were uniaxially hot-pressed at 25 MPa (900 ºC 12 h), under air, with a final furnace cooling to obtain disks of about 30 mm diameter and 3 mm thickness. For this process, these disks were placed between two

Ag foils, and two alumina blocks. Finally, these samples were cut into pieces with adequate dimensions for their structural and thermoelectric characterization.

2.2. Structural and microstructural characterization

Phase identification was performed by powder X-ray diffraction (XRD) using a PANalytical X'Pert MPD Philips diffractometer (CuKα radiation, λ=1.54056 Å) at 40 kV and 30 mA, with a step 0.02 º in 1 s, in the 2θ angle range of 10 – 60 º. Phase indexation was made using the JCPDS database. Texture analysis (pole figure) to quantify the grain alignment degree, was performed on both samples using a diffractometer Philips MRD with Cu radiation X-ray point focus configuration, a crossed slit collimator in the incident beam and a parallel plate collimator in the diffracted beam. The data were acquired using the diffraction peak at 37.1 degrees, corresponding to the (200) crystallographic plane.

Microstructural characterization was performed on longitudinal surfaces and transversal fractures of the samples using a Field Emission Scanning Electron Microscope (FESEM, Zeiss Merlin) equipped with an energy dispersive spectrometry (EDS) analysis system. In order to obtain more guidelines on the morphology and microstructural features, surface sections of representative samples were polished and chemically etched in HCl (6 M) for 2 s.

Apparent density measurements have been performed after each processing step to obtain preliminary information on the microstructural evolution in the samples. At least three samples were measured for three times to get corresponding average values with reasonable accuracy.

High-resolution SEM images in secondary emission mode, used as references for AES analysis, were obtained using the same equipment operating in SEM mode (30 keV, 2 nA, working distance = 23 mm).

2.3. XPS and AES characterization

The surface atomic composition and chemical environment of elements at the surface were determined by X-ray photoelectron spectroscopy (XPS) analysis. A Thermo K-alpha system with a hemispherical analyser and a microfocused (analysis area was ca. 200 mm²) monochromatized radiation Al Kα line (1486.6 eV) operating at 75 W was used for XPS characterization. The residual pressure in the spectrometer was 1 10^{-9} mbar. A neutralizer gun was used to prevent surface charging, by spraying low energy electrons and Ar ions over the sample surface. The spectrometer pass energy was set to 200 eV for survey spectrum and to 20 eV for core peak records. The treatment of core peaks was carried out using a nonlinear Shirley-type background. We have used a weighted least squares fitting method, considering 70 % Gaussian and 30 % Lorentzian line shapes, to deconvolute the experimental spectra and to fit the peak positions and areas. The core peaks spectra were calibrated by setting the binding energies of the C1s peak assigned to adventitious carbon at 285.0 eV. The quantification of surface composition was based on Scofield's relative sensitivity factors [26].

Before AES analyses, the samples were cross-cut with a JEOL Cross-Polisher (JEOL Ltd.), using ion-milling polishing method. A stainless steel shield plate was used to protect one-half of the sample, while the non-protected area was etched with an Ar$^+$-ion beam (6 keV). A very clean polished surface was obtained due to the grazing angle (< 2

° to the surface) leading to limited implantation of Ar^+ ions into the etched sample. After cutting, the samples were mounted on a sample holder for Auger analyses.

Auger Electron Spectroscopy (AES) analyses were carried out with a JEOL JAMP 9500F Auger spectrometer (JEOL Ltd, Tokyo, Japan) operating under ultra-high vacuum (UHV) conditions (pressure < 2 10^{-7} Pa). The UHV equipment was a Schottky field emission Auger electron spectrometer (FE-AES) dedicated to very high spatial resolution (~ 10 nm probe diameter) analysis and high brightness. The hemi-spherical electron analyzer coupled with a multichannel detector (7 channeltrons) offered ideal settings for energy resolved Auger analysis.

2.4. Thermoelectric characterization

Electrical resistivity and Seebeck coefficient were simultaneously measured by the standard four-probe DC technique in a LSR-3 system (Linseis GmbH). The samples were measured in the steady state mode at temperatures ranging from 50 to 800 ºC under He atmosphere. Thermal conductivity was determined, in the same direction of the Seebeck and electrical resistivity measurements, using the photothermal radiometry technique (PTR) under air atmosphere. Here, a modulated laser beam (at 532 nm wavelength generated by an internally-modulated Ventus DPSS laser source) is absorbed by the studied material placed on a thermally semi-infinite substrate. The light beam is beforehand enlarged by a telescopic arrangement to ensure one-dimensional heat propagation inside the investigated system. Based on modulation frequency dependence of the temperature distribution, one can calculate the thermal parameters of the material. In the case of opaque samples and for small temperature variations, infrared total emittance radiated by the material is then directly proportional to its

surface temperature [27]. This infrared radiation was then collected as a function of the modulation frequency using a Mercury Cadmium Tellurium (MCT) detector cooled down to liquid nitrogen temperature (Teledyne Judson Technologies J15D12-M204-S01M-60). Pre-amplified output electric signal (Teledyne Judson Technologies PA 300) was processed in a lock-in amplifier (EG&G 7260). Thermal parameters were calculated based on the relationships with the surface temperature, using the procedure described in more detail elsewhere [28]. Thermal diffusivity (α) and effusivity (e) were extracted from the normalized phase of the PTR signal. Thermal conductivity (κ) is then calculated using the equation $\kappa = e \sqrt{\alpha}$.

ZT values were calculated at 25-150 ºC, using power factor ($PF = S^2/\rho$) and thermal conductivity data. In addition, the ZT values have been estimated at higher temperatures, considering κ unchanged with temperature, and compared to the best up-to-date literature data. Taking into account that the thermal conductivity of $Ca_3Co_4O_9$-based materials decreases on heating [29-30], the real κ values are expected to be lower than the estimated ones, which means that real TE performance of the studied materials at high temperatures can be notably higher.

3. Results and discussion
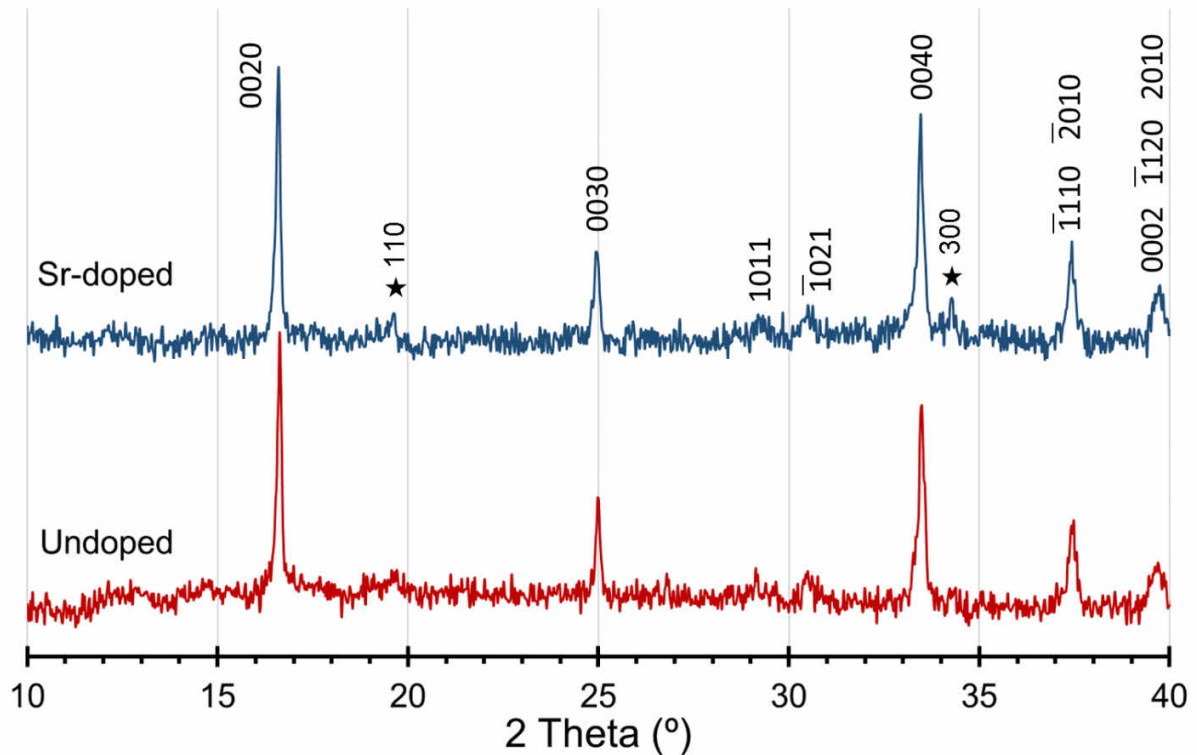
3.1. XRD characterization

9

Figure 1. Powder XRD patterns of undoped and Sr-doped $Ca_3Co_4O_9$ samples. Diffraction planes indicate the reflections corresponding to $Ca_3Co_4O_9$ phase, while * identify those associated to $Ca_3Co_2O_6$ one

According to the powder XRD patterns shown in Fig. 1 (from 10 to 40 º, for clarity), both undoped and Sr-doped samples possess similar phase composition, together with nearly equal ratios between intensities of the relevant peaks. Major peaks correspond to the $Ca_3Co_4O_9$–based phase indexed indexed in accordance with the incommensurate superstructure, described in [31] Despite noticeable peaks broadening, possibly due to the microstructural effects described below, the tendency for peaks shifting towards lower 2θ angles is evident for Sr- containing composition indicating the substitution of Ca^{2+} by larger Sr^{2+} cations. On the other hand, some minor peaks corresponding to the $Ca_3Co_2O_6$ phase were also observed [32,33]. The presence of this secondary phase is in agreement with the available literature [19,34,35]. The most intense peaks are

10

associated with (00l0) planes, likely provided with preferential orientation of grains due to their plate-like shape. These observations are clearly in agreement with previously reported results on solid state sintered materials in this Sr-doped system [21]. Representative poles figure obtained for the $Ca_3Co_4O_9$ sample surface is shown in Fig. SI1. The results indicate significant grain alignment in the samples, with their *ab*-planes being parallel to the sample surface. Moreover, the grain alignment is very similar in both cases (around 13 º misalignment), pointing out to a negligible effect of Sr doping on the grains orientation.

3.2. Microstructure

Fig. 2a shows a representative micrograph of the microstructure after uniaxial hot-pressing process, taken at a transversal fractured section of undoped samples. As it can be observed in the picture, in spite of the conventional sintering procedure preceding the hot-pressing process, the plate-like grains show a relatively good orientation of their *ab*-planes perpendicular to the applied pressure, in agreement with the pole figures discussed above. The grains show a significant aspect ratio, with the grain sizes exceeding 5 µm along the *a*- and *b*-directions. These results are in clear agreement with the pole figures shown in the supplementary information, confirming the presence of preferential orientation of the plate-like grains in the prepared samples.
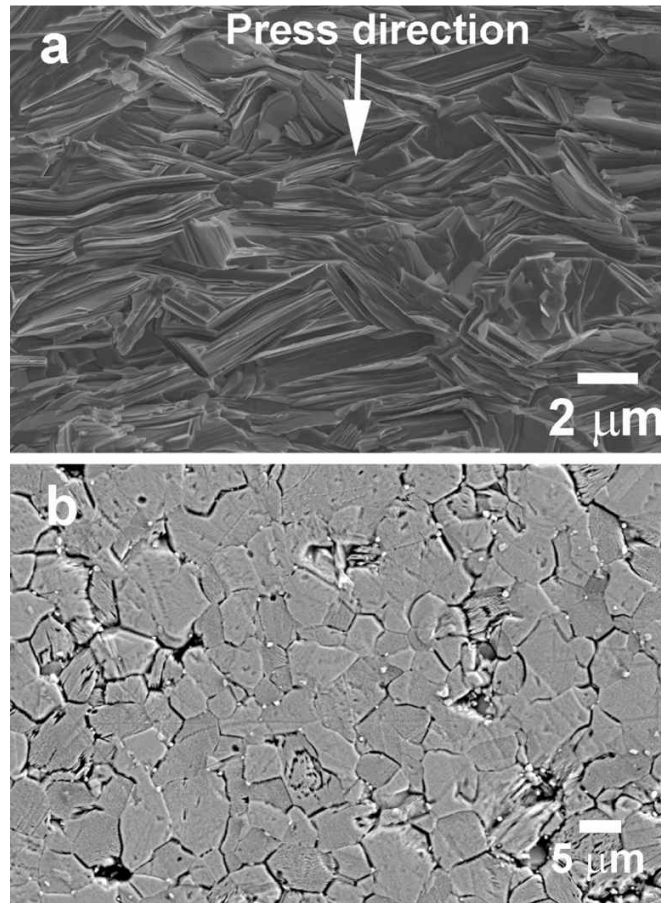
Figure 2. Representative SEM micrographs taken on a) fractured transversal sections of $Ca_3Co_4O_9$ samples (The arrow indicates the pressure direction in the cold and the hot uniaxial pressing processes); and b) polished surface of Sr-doped samples after chemical etching.

Fig. 2b, shows a representative view of the polished surface of the Sr-substituted samples after etching. It suggests a low level of porosity in these samples, while big pores observed in the micrograph are most likely provided by the polishing procedure. Moreover, individual grains larger than 5 μm can be seen, in accordance with the previous observations. EDS analysis performed in several points and areas along the samples has shown that they are formed by single $Ca_3Co_4O_9$, and $Ca_{2.93}Sr_{0.07}Co_4O_9$ phases in the undoped and Sr-doped samples, respectively. On the other hand, no

$Ca_3Co_2O_6$ phase has been detected with this technique, most likely due to its low amount, as observed in the powder XRD patterns. The latter indicates that the selected processing conditions are adequate to produce nearly single thermoelectric phase with highly oriented grains in all samples.

Table 1: Relative density of samples after different processing steps, together with their errors.

	Relative density (%)		
	Pressed	Sintered	Hot-pressed
$Ca_3Co_4O_9$	62.0 ± 2.7	75.1 ± 1.3	95.1 ± 0.7
$Ca_{2.97}Sr_{0.03}Co_4O_9$	60.0 ± 2.1	74.2 ± 1.0	95.0 ± 0.5

In order to confirm the microstructural observations suggesting very low porosity in these samples, density measurements were performed for both types of samples using the Archimedes method. The relative mean density evolution after each processing step (pressing, sintering, and hot-pressing) was determined using 4.68 g/cm^3 as reference for theoretical one [36], and displayed in Table 1, together with their respective errors. Both samples possess very close relative densities after each processing step, as it might be expected from similar chemical composition and precursors. The conventional sintering procedure only slightly increases the samples density due to the relatively low sintering temperatures. This limitation of sintering temperature for $Ca_3Co_4O_9$ phase is known to be imposed by its stability limit (around 920 ºC), while the minimum temperature to form liquid phase corresponds to ~1350 ºC [37]. This limitation leads to typical density values lower than 80 % in the available literature [38,39]. Therefore, it is necessary to use other processes to produce highly-dense $Ca_3Co_4O_9$-based materials, including two-step sintering [40], melt-solidification [41], SPS [42], or hot-pressing [14], which allow reaching densities close to the theoretical one (see Table 1).

3.3. XPS and AES analysis

In addition to XRD analysis, which is representative of materials bulk, surface techniques as XPS and AES have been used to provide complementary information and some insights on the local phase composition, the elemental spatial distribution and the electronic structure of materials. Concerning XPS, the spectra were recorded for Ca 2p, Co 2p, O 1s, Sr 3d and C 1s regions, corresponding to binding energies (B.E.) and atomic percentages shown in Table SI1.

The Co 2p core peaks are represented in Fig. 3a. The spectra consist in two main components Co $2p_{3/2}$ and Co $2p_{1/2}$ located at 780.3 eV and 794.8 eV, respectively, with satellite peaks at 789.6 eV and 804.7 eV. It is well known that the shape and characteristics of the Co 2p spectra for trivalent and tetravalent states are very similar. Nonetheless, from the paper of Dahéron et al. [43], it is possible determining the average Co oxidation state by considering the satellite relative area of the main Co 2p peak. The estimation has been +3.3, higher than the obtained in sintered materials [25]. The shoulders at the high-binding-energy side of Co $2p_{3/2}$ and Co $2p_{1/2}$ main peaks can be attributed to the interaction between the CoO_6 clusters [44] and are not linked to the appearance of additional oxidation states.

The Ca 2p spectra (Fig. 3b) consists in two peaks (Ca $2p_{3/2}$ and Ca $2p_{1/2}$) separated by 3.5 eV due to the spin orbit coupling. The spectra can be decomposed into two doublets associated to: i) calcium in the rock salt layer in a Ca-O environment [45] (B.E. Ca $2p_{3/2}$ = 345.7 eV) and ii) calcium carbonate (B.E. (Ca $2p_{3/2}$) = 346.8 eV) [46].
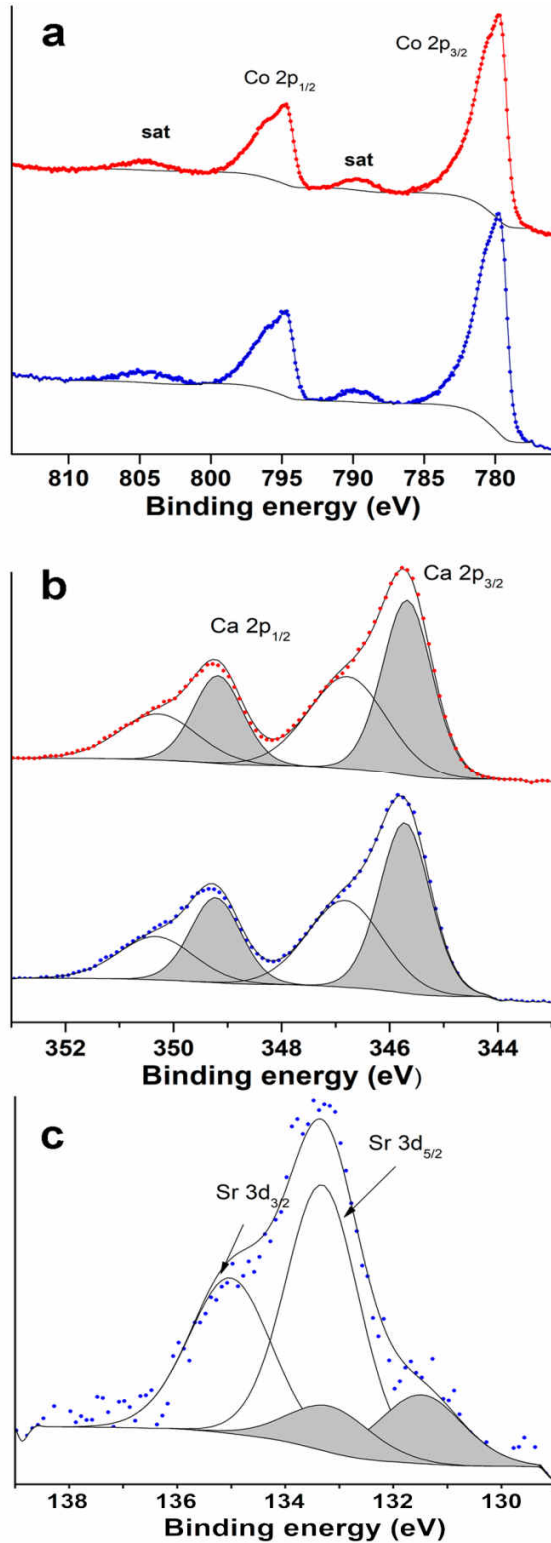
Figure 3: XPS spectra obtained in undoped (-); and Sr-doped (-) $Ca_3Co_4O_9$ samples, for a) Co 2p; b) Ca 2p; and c) Sr 3d spectra in Sr-doped ones.

In Sr-doped material, the overall shape of the Co 2p core peak is retained, no broadening of the main peak towards higher binding energies was observed. Moreover, no evolution of the oxidation state has been detected by considering the area ratio between the satellite and the main peak. On the other hand, two chemical environments can be identified for Sr (Fig. 3c). The main part of the signal is attributed to Sr in carbonate environment (B.E. Sr $3d_{5/2}$ = 133.4 eV [47]), and Sr^{2+} in oxygenated environment in the $Ca_{2.93}Sr_{0.07}Co_4O_9$ phase (B.E ($Sr\ 3d_{5/2}$) = 131.5 eV). Thus, only a limited part of strontium (25 % of the Sr 2p entire signal) seems to substitute Ca in the rock salt layer.

The composition of the materials obtained from XPS analyses is $Ca_{2.6\pm0.1}Co_4O_{8.1\pm0.1}$ for the non-doped and $Ca_{2.9\pm0.1}Sr_{0.1\pm0.1}Co_4O_{8.7\pm0.1}$ for the Sr-doped materials, which is close to the composition issued from the EDS analyses. It is important to highlight that the deviation of the surface composition from the nominal one is usually reported in XPS quantitative analyses, explaining the compositional deviation from the nominal one.
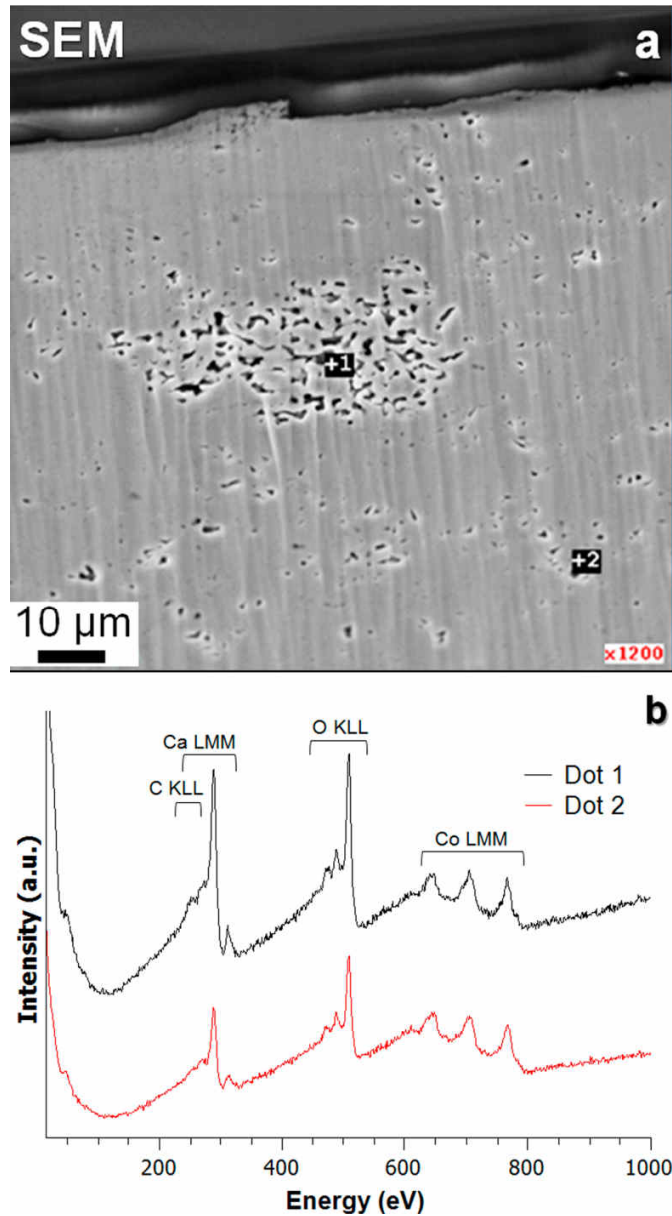
Figure 4: Auger analyses of two target dots in the undoped material: (a) SEM image with the location of the two dots and (b) the corresponding Auger spectra.

AES analyses were performed to study the nanoscale elemental spatial distribution on materials surfaces for the undoped and Sr-doped samples. Two single point analyses were carried out on the undoped sample, within (dot 1) and outside (dot 2) a holed region (Fig. 4a). As displayed on the corresponding Auger spectra (Fig. 4b), Co LMM

and O KLL transitions are clearly identifiable at 320-703 eV and 460-530 eV, respectively, in both dots. In addition, overlapped transitions of Ca LMM and C KLL are also observed at 240-330 eV. Due to this overlapping and the high intensity of Ca signal, carbon transition could not be correctly extracted from the curve. However, the comparison of the two spectra shows a higher peak-to-peak intensity ratio between Ca/C and Co transitions within the holed region (dot 1). Such observation can be corroborated by AES chemical mapping, for a specific area including a holed region (Fig. SI2) showing higher Ca and O detection and lower Co signal within the porous region. These results are in good agreement with the presence of $CaCO_3$ environments, previously identified by XPS. Such environments are preferentially located within holed inclusions in the material.
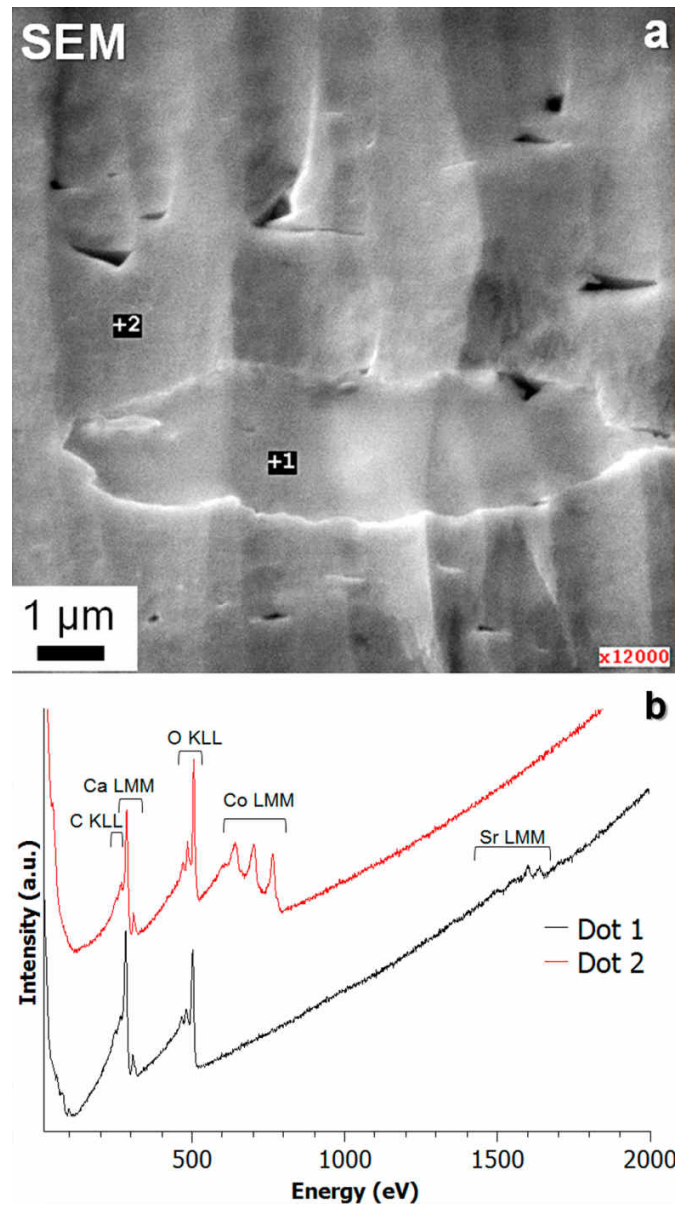
Figure 5: Auger analyses of two target dots for the Sr-doped material: (a) SEM image showing a Sr-inclusion and the location of the two target dots and (b) the corresponding Auger spectra

In the Sr-doped material, Sr rich inclusions have been clearly identified by Auger spectroscopy. In Fig. 5a, a SEM micrograph pointing out a Sr-rich inclusion is shown, together with the location of two target dots, where Auger analysis was performed. The corresponding spectra of the two dots have been recorded (Fig. 5b) giving Ca, C and

Co transitions within the same energy ranges found in the undoped material. Moreover, a Sr LMM transition at 1475-1660 eV for dot 1 is also identified. Such observations were confirmed by AES mapping for which Sr signal (Fig. SI3) is only detected within the inclusion whereas Co is detected outside (overlay Fig. SI3). In agreement with the XPS data, such inclusion corresponds to $SrCO_3$ phase due to the reactivity of Sr with moisture and CO_2 (Sr in the $Ca_{2.93}Sr_{0.07}Co_4O_9$ phase outside the inclusion is under the detection limit of Auger signal due to its low content, 0.3 at. %). These strontium carbonates can sequester Ca from the $Ca_3Co_4O_9$ phase, producing these large particles. In particular, thermodynamic stability of alkaline-earth carbonates increases with cation radii [48].

It should be noticed that such interactions impose some limitations on the applicability of the XPS, which is essentially surface technique, for analysis of the local atomic contents for the constituting elements. Still, some guidelines can be obtained from the results presented in Table SI1.

For both undoped and Sr-doped samples a significant deviation from the nominal Ca(Sr):Co ratio was observed (Sr/Co=0.1; Ca/Co ~ 1.2 from XPS analyses), suggesting a Ca(Sr) excess at the surface. This enrichment is, again, driven by the tendency of these elements to form carbonates, corroborating the above conclusions drawn from the Auger spectroscopy results. The presence of calcium and strontium carbonate is thus mainly on surface, which explains that diffraction lines related to those phases have not been detected on XRD patterns. Thus, the actual substitution level of Ca^{2+} for Sr^{2+} may be strongly affected by the residual porosity irrespectively of the used processing conditions, unless they provide nearly 100% dense material.

3.4. Thermoelectric properties

Electrical resistivity measurements as a function of temperature have been performed both on undoped and Sr-doped samples, and the results are displayed in Fig. 6a, together with their estimated error (4%) in agreement with previously determined errors in this measuring system [49]. They remain nearly constant between room temperature (RT) and 200 ºC, and decrease at higher temperatures, showing a semiconducting-like behaviour (dρ/dT ≤ 0). Moreover, the Sr-doped samples display lower resistivity values than the undoped ones in the whole measured temperature range, in agreement with previous studies [21]. The minimum resistivity values at 800 ºC (6.5 mΩ cm), are close to those obtained for textured materials prepared through SPS (6 mΩ cm) [50], edge-free SPS (7 mΩ cm) [51], and lower than the obtained in hot-pressed specimens (25 mΩ cm) [14], or in classically sintered samples with the same composition (15 mΩ cm) [21]. Several factors may be responsible for high electrical performance, including high density and minor impurities content, as compared to other works cited above (only Sr and Ca carbonates have been observed at the surfaces (5 nm in depth) with XPS and Auger techniques coming from superficial carbonation of samples), the relatively high Co valence, significant grain alignment, and good electrical connectivity between the grains. Moreover, these results also suggest a slight oxygen loss in the samples, as can be observed when comparing these results with the obtained through SPS. As it is well known, SPS process uses graphite sheets to press the samples during the sintering procedure, possibly creating a reducing atmosphere around the sample and slightly decreasing the oxygen content due to the very limited process duration. On the other hand, the long hot-pressing procedure should also modify the oxygen content in the

surface. In any case, the main factor for the low electrical resistivity measured in these samples is associated to the good grain orientation and grains connectivity obtained through the hot-pressing effect.
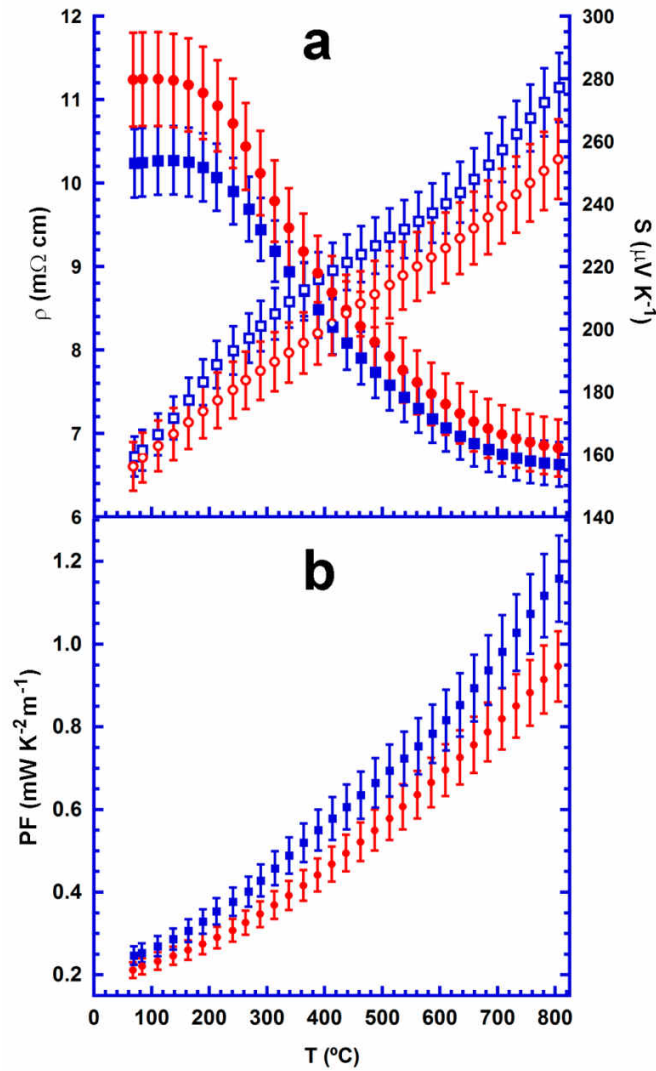

Figure 6: a) Temperature dependence of the electrical resistivity (filled symbols) and Seebeck coefficient (empty symbols) for the undoped (●, ○); and Sr-doped (■, □) $Ca_3Co_4O_9$ samples, together with their errors; b) Temperature dependence of the power factor for the undoped (●); and Sr-doped (■) $Ca_3Co_4O_9$ samples, together with their error.

Fig. 6a also shows the variation of the Seebeck coefficient with temperature obtained in undoped and Sr-doped samples, together with a previously estimated error (4 %) [49]. The values are positive in the whole measured temperature range, confirming a dominant p-type electronic conduction mechanism. The values of Seebeck coefficient increase with temperature, showing similar behaviour in both samples, while being notably higher for the Sr-doped material, especially at high temperatures. The data at nearly room temperature suggest similar concentration of charge carriers for undoped and Sr-doped materials, in agreement with Koshibae's expression [52], as their S values at RT are nearly the same; the same conclusion follows from the oxidation state extracted from XPS analyses ($Co^{+3.3}$). When considering the room temperature values measured in these samples (around 150 μV/K), it is clear that they are much lower than the predicted through Koshibae's expression (about 200 μV/K) [53]. This is a typical trend already observed in previous works on $Ca_3Co_4O_9$, the theoretical values are much higher than the experimentally determined [54,55]. In any case, the slightly different RT values obtained for all samples indicate that small Sr addition softly affects the $Ca_3Co_4O_9$ conduction band [56]. These S values, measured at low temperatures, are only slightly higher than the obtained in pure and Sr-doped classically sintered samples (around 135 μV/K) [21], and can be due to the long hot-pressing process which can modify the oxygen content in the samples surface, as previously discussed for the electrical resistivity values. On the other hand, when evaluating the maximum S values at 800 ºC (275 μV/K), it is clear that they are much higher than the usual values reported in the literature for textured materials produced through SPS (165 μV/K) [50], or the classically sintered compounds (220 μV/K) [21].

The fact that the values of Seebeck coefficient measured for Sr-containing material are noticeably above those for pure $Ca_3Co_4O_9$ sample, especially at high temperatures seems counterintuitive, if considering the isovalent nature of the substitution and roughly similar average cobalt oxidation states in these compositions, at least at low temperatures as confirmed by the XPS results. A similar but weak increase in the Seebeck coefficient was previously observed for $[(Sr_{1-x}Ca_x)_2(O,OH)_2]_q[CoO_2]$ on calcium for strontium substitution and attributed to the effects exerted by changes in misfit parameter [57]. The results obtained in [58] for $Ca_{3-x}Sr_xCo_4O_9$ single crystals also suggest higher Seebeck coefficient in Sr-containing materials. In this case, the latter was attributed to the negative chemical pressure effects owing to the difference in cation size, which results in strengthening the two-dimensionality of the system and enhancing the effective mass of the charge carriers confined in the CoO_2 layer. The work [58], however, emphasizes, that such effects are vanished in polycrystals by averaging the large anisotropy of the $Ca_3Co_4O_9$ crystal lattice. This underlines a necessity to apply a specific processing route to gain the benefits from the effects of Sr substitution on Seebeck coefficient. The discussed effects are believed to be a reason for the relatively high Seebeck coefficients observed in the present work, where complementary modified hot pressing process allows producing higher anisotropy in the bulk samples due to texturing.

The temperature dependence of PF, calculated from the electrical resistivity and Seebeck coefficient data, is presented in Fig. 6b, together with an estimated error of around 9 %. PF increases with temperature showing a nearly linear trend, reaching the highest values reported so far, in the best of our knowledge, for $Ca_3Co_4O_9$

polycrystalline materials. This enhancement is mostly provided by very high Seebeck coefficient in textured materials, as discussed above. Substitution with strontium further improves PF values up to 20 % in the whole measured temperature range. The highest values at 800 ºC (1.16 mW/K^{2}m) are nearly three times higher than the best ones reported in the literature for the materials produced via different techniques (about 0.43 mW/K^{2}m) [25,40,51].
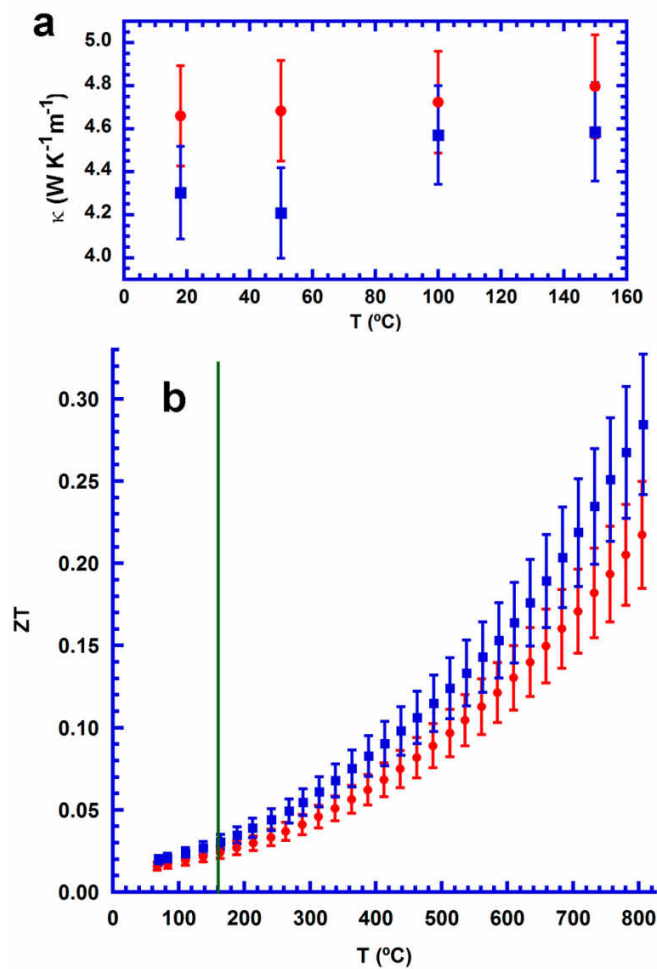

Figure 7: a) Temperature dependence of thermal conductivity for undoped (●); and Sr-doped (■) samples, together with their errors; and b) Temperature dependence of ZT for undoped (●); and Sr-doped (■) samples, together with their error. The vertical line is a guide for eyes to separate the calculated (low temperatures) and estimated values (high temperatures), considering thermal conductivity constant in the whole temperature range.

Thermal conductivity of hot pressed undoped and Sr-doped $Ca_3Co_4O_9$ samples were evaluated at 18-150 °C using photothermal radiometry technique (PTR). This method was selected mainly taking into account the experimental difficulties associated with reliable measurements for small rod-like samples. Fig. SI4 depicts the temperature dependence of the thermal effusivity and diffusivity for undoped and Sr-doped $Ca_3Co_4O_9$ samples. From these data, it is easy to observe that Sr-doping decreases both parameters. Consequently, thermal conductivity, calculated using these data and presented in Fig. 7a, together with their 5 % error [49], in the whole studied temperature range, is lower for $Ca_{2.93}Sr_{0.07}Co_4O_9$ than for the undoped $Ca_3Co_4O_9$, in spite of a higher electrical conductivity. This observation clearly indicates that Sr-doping provides larger contribution to suppress the lattice thermal conductivity if taking into account the corresponding increase in its electronic counterpart, as it might be expected from its higher electrical conductivity. Phonon scattering at point defects is facilitated by introducing heavier elements. Moreover, Sr-doping is expected to widen the phonon scattering spectrum, as the size of point defects is significantly smaller than the scale of misfit layers, mainly responsible for the relatively low thermal conductivity in $Ca_3Co_4O_9$-based materials. Another contribution to suppressing the lattice thermal conductivity is expected from the different ionic radius of Ca^{2+} and Sr^{2+} cations, which determines the magnitude of the lattice misfit and affects the dynamics of interference between CoO_2 and rock-salt layers [59]. For both materials, thermal diffusivity is decreasing and thermal conductivity stays roughly constant in the range of studied temperatures (about 4.7, and 4.4 W/K m, for the undoped, and Sr-doped samples, respectively).

Based on obtained thermal conductivity values, ZT has been calculated from room temperature to 160 ºC, and estimated for higher temperatures, where, assuming the usual behaviour of $Ca_3Co_4O_9$ and other thermoelectric oxides, the thermal conductivity should decrease. The calculated values are shown in Fig. 7b, together with their error (15 %) [49], where it can be observed that Sr doping clearly improved the performances of samples (close to 50 % at 800 ºC), when compared with the undoped $Ca_3Co_4O_9$. On the other hand, in spite of the impressive improvements achieved in electrical performance, the unusually high thermal conductivities led to lower ZT values than one may expect based on the high PF previously discussed. The maximum values obtained at 800 ºC (0.29) in the Sr-doped samples are slightly lower than for those prepared using a transient liquid phase (0.35) [60]. On the contrary, at 600 ºC, ZT of Sr-doped materials (0.16) is significantly higher than the reported in the literature (0.07) for textured materials [14,30]. Once again, it is necessary to note that the high temperature ZT values are most probably underestimated due to the assumption of a constant thermal conductivity value above 160 ºC.

From these data, it is clear that the procedure used in this work leads to very attractive electrical properties in $Ca_3Co_4O_9$-based materials. Besides this, the thermal conductivity also appears to decrease on substitution with strontium. Such simultaneous improvement of different thermoelectric properties represents a significant challenge, but it was achieved in the present work by combined effects imposed by substitution and processing. This is a very promising result for materials composed of micrometer-sized grains, as such independent tunning of all thermoelectric parameters has been mostly achieved in nanostructured materials. Furthermore, it seems evident that

increasing ZT values can be further promoted by additional doping with rare earth elements, which, besides their influence on decreasing thermal conductivity, are not expected to significantly modify the electrical properties.

4. Conclusions

This work demonstrates how highly-performing $Ca_3Co_4O_9$ thermoelectric materials can be produced through a modified hot-pressing process combined with doping. Microstructural studies have revealed significant grain orientation, relatively large grain sizes, and low porosity. Density measurements confirmed the high density of samples (around 95 % of the theoretical one). XPS analysis has demonstrated that Sr doping does not modify the $Ca_3Co_4O_9$ valence band, while Auger spectroscopy showed that Sr-doping enhanced the samples reactivity with moisture, leading to Sr and Ca carbonates formation, especially when residual porosity is present in the sample. Thermoelectric properties are significantly improved by Sr-doping, provided by lower electrical resistivity and thermal conductivity, and higher Seebeck coefficient, compared to the undoped samples. The power factor of Sr-containing samples was found to be the highest reported so far in this system in polycrystalline bulk materials, mostly due to an unusual enhancement in Seebeck coefficient. In spite of the great improvement of PF, ZT values are only around the best reported in the literature (around 0.29), due to their high thermal conductivity.

References

1. D. M. Rowe, in Thermoelectrics handbook: macro to nano, ed. D. M. Rowe, CRC press, Boca Raton, FL, 2005.

2. G. Mahan, B. Sales, J. Sharp, Thermoelectric materials: New approaches to an old problem, *Phys. Today* 50 (1997) 42–47.

3. H. Naito, Y. Kohsaka, D. Cooke, H. Arashi, Development of a solar receiver for a high-efficiency thermionic/thermoelectric conversion system, *Sol. Energy* 58 (1996) 191–195.

4. C. M. Kim, Y. J. Hwang, Y. H. Ryu, US Patent US6393842. May, 2002.

5. H. Wang, J. Hwang, M. L. Snedaker, I.-H. Kim, C. Kang, J. Kim, G. D. Stucky, J. Bowers, W. Kim, High Thermoelectric Performance of a Heterogeneous PbTe Nanocomposite, *Chem. Mater.* 27 (2015) 944–949.

6. J. A. Santamaria, J. Alkorta, J. G. Sevillano, Microcompression tests of single-crystalline and ultrafine grain Bi_2Te_3 thermoelectric material, J. *Mater. Res.* 30 (2015) 2593–2604.

7. I. Terasaki, Y. Sasago, K. Uchinokura, Large thermoelectric power in $NaCo_2O_4$ single crystals, *Phys. Rev. B* 56 (1997) 12685–12687.

8. F. Kahraman, M. A. Madre, Sh. Rasekh, C. Salvador, P. Bosque, M. A. Torres, J. C. Diez, A. Sotelo, Enhancement of mechanical and thermoelectric properties of $Ca_3Co_4O_9$ by Ag addition, *J. Eur. Ceram. Soc.* 35 (2015) 3835 -3841.

9. K. Miyazawa, F. Amaral, A. V. Kovalevsky, M. P. F. Graca, Hybrid microwave processing of $Ca_3Co_4O_9$ thermoelectrics, *Ceram. Int.* 42 (2016) 9482–9487.

10. F. Delorme, C. F. Martin, P. Marudhachalam, G. Guzman, D. O. Ovono, O. Fraboulet, Synthesis of thermoelectric $Ca_3Co_4O_9$ ceramics with high ZT values from a $Co^{II}Co^{III}$-Layered Double Hydroxide precursor, *Mater. Res. Bull.* 47 (2012) 3287–3291.

11. R. Funahashi, I. Matsubara, H. Ikuta, T. Takeuchi, U. Mizutani, S. Sodeoka, An oxide single crystal with high thermoelectric performance in air, *Jpn. J. Appl. Phys.* 39 (2000) L1127–L1129.

12. Y. Zhang, J. Zhang, Q. Lu, Synthesis of highly textured $Ca_3Co_4O_9$ ceramics by spark plasma sintering, *Ceram. Int.* 33 (2007) 1305–1308.

13. J. G. Noudem, D. Kenfaui, D. Chateigner, M. Gomina, Granular and Lamellar Thermoelectric Oxides Consolidated by Spark Plasma Sintering, *J. Electron. Mater.* 40 (2011) 1100–1106.

14. H. Wang, X. Sun, X. Yan, D. Huo, X. Li, J.-G. Li, X. Ding, Fabrication and thermoelectric properties of highly textured $Ca_9Co_{12}O_{28}$ ceramic, *J. Alloys Compds.* 582 (2014) 294–298.

15. H. Itahara, C. Xia, J. Sugiyama, T. Tani, Fabrication of textured thermoelectric layered cobaltites with various rock salt-type layers by using β-$Co(OH)_2$ platelets as reactive templates, *J. Mater. Chem.* 14 (2004) 61–66.

16. Sh. Rasekh, G. Constantinescu, M. A. Torres, M. A. Madre, J. C. Diez, A. Sotelo, Growth rate effect on microstructure and thermoelectric properties of melt grown $Bi_2Ba_2Co_2O_x$ textured ceramics, *Adv. Appl. Ceram.* 111 (2012) 490–494.

17. N. M. Ferreira, Sh. Rasekh, F. M. Costa, M. A. Madre, A. Sotelo, J. C. Diez, M. A. Torres, New method to improve the grain alignment and performance of thermoelectric ceramics, *Mater. Lett.* 83 (2012) 144–147.

18. X. Y. Song, Y. Chen, S. Chen, E. Barbero, E. L. Thomas, P. Barnes, Significant enhancement of electrical transport properties of thermoelectric $Ca_3Co_4O_{9+\delta}$ through Yb doping, *Solid State Commun.* 152 (2012) 1509–1512.

19. H. Liu, G. C. Lin, X. D. Ding, J. X. Zhang, Mechanical relaxation in thermoelectric oxide $Ca_{3-x}Sr_xCo_4O_{9+\delta}$ (x=0, 0.25, 0.5, 1.0) associated with oxygen vacancies, *J. Solid State Chem.* 200 (2013) 305–309.

20. G. Kirat, M. A. Aksan, Sh. Rasekh, M. A. Madre, J. C. Diez, A. Sotelo, Decrease of $Ca_3Co_4O_{9+\delta}$ thermal conductivity by Yb-doping, *Ceram. Int.* 41 (2015) 12529–12534.

21. G. Constantinescu, Sh. Rasekh, M. A. Torres, J. C. Diez, M. A. Madre, A. Sotelo, Effect of Sr substitution for Ca on the $Ca_3Co_4O_9$ thermoelectric properties, *J. Alloys Compds.* 577 (2013) 511–515.

22. F. Delorme, C. Fernandez Martin, P. Marudhachalam, D. Ovono Ovono, G. Guzman, Effect of Ca substitution by Sr on the thermoelectric properties of $Ca_3Co_4O_9$ ceramics, *J. Alloys Compds.* 509 (2011) 2311–2315.

23. S. Li, R. Funahashi, I. Matsubara, H. Yamada, K. Ueno, S. Sodeoka, Synthesis and thermoelectric properties of the new oxide ceramics $Ca_{3-x}Sr_xCo_4O_{9+\delta}$ (x=0.0–1.0), Ceram*. Int.* 27 (2001) 321–324.

24. L. B. Wang, A. Maignan, D. Pelloquin, S. Hebert, B. Raveau, Transport and magnetic properties of $Ca_{3-x}Sr_xCo_4O_9$, *J. Appl. Phys.* 92 (2002) 124–128.

25. A. Sotelo, Sh. Rasekh, M. A. Torres, P. Bosque, M. A. Madre, J. C. Diez, Effect of synthesis methods on the $Ca_3Co_4O_9$ thermoelectric ceramic performances, *J. Solid State Chem.* 221 (2015) 247–254.

26. J. H. Scofield, Hartree-Slater Subshell Photoionization Cross-sections at 1254 and 1487 eV, *J. Electron. Spectrosc. Relat. Phenom.* 8 (1976) 129–137.

27. P. E. Nordal, S. O. Kanstad, Photothermal radiometry. *Phys. Scr.* 20 (1979) 659–662.

28. M. Depriester, P. Hus, S. Delenclos, A. H. Sahraoui, New methodology for thermal parameter measurements in solids using photothermal radiometry, *Rev. Sci. Instr.* 76 (2005) 074902.

29. N. Prasoetsopha, S. Pinitsoontorn, T. Kamwanna, V. Amornkitbamrung, K. Kurosaki, Y. Ohishi, H. Muta, S. Yamanaka, The effect of Cr substitution on the structure and properties of misfit-layered $Ca_3Co_{4-x}Cr_xO_{9+\delta}$ thermoelectric oxides, *J. Alloys Compds.* 588 (2014) 199–205.

30. D. Kenfaui, B. Lenoir, D. Chateigner, B. Ouladdiaf, M. Gomina, J. G. Noudem, Development of multilayer textured $Ca_3Co_4O_9$ materials for thermoelectric generators: influence of the anisotropy on the transport properties, *J. Eur. Ceram. Soc.* 32 (2012) 2405–2414.

31. Y. Miyazaki, M. Onoda, T. Oku, M. Kikuchi, Y. Ishii, Y. Ono, Y. Morii, T. Kajitani, Modulated structure of the thermoelectric compound $[Ca_2CoO_3]_{0.62}CoO_2$, *J. Phys. Soc. Jpn.* 71 (2002) 491–497

32. E. Woermann, A. Muan, Phase equilibria in the system CaO–cobalt oxide in air, *J. Inorg. Nucl. Chem.* 32 (1970) 1455–1459.

33. C. H. Hervoches, H. Okamoto, A. Kjekshus, H. Fjellvag, B. C. Hauback, Crystal structure and magnetic properties of the solid-solution phase $Ca_3Co_{2-v}Mn_vO_6$, *J. Solid State Chem.* 182 (2009) 331–338.

34. F. Delorme, P. Diaz-Chao, E. Guilmeau, F. Giovannelli, Thermoelectric properties of $Ca_3Co_4O_9$–Co_3O_4 composites, *Ceram. Int.* 41 (2015) 10038–10043.

35. N. Puri, R. P. Tandon, A. K. Mahapatro, Fully dense hot pressed calcium cobalt oxide ceramics, *Ceram. Int.* 44 (2018) 6337–6342.

36. A. C. Masset, C. Michel, A. Maignan, M. Hervieu, O. Toulemonde, F. Studer, B. Raveau, J. Hejtmanek, Misfit-layered cobaltite with an anisotropic giant magnetoresistance: $Ca_3Co_4O_9$, *Phys. Rev. B* 62 (2000) 166–175.

37. D. Sedmidubsky, V. Jakes, O. Jankovsky, J. Leitner, Z. Sofer, J. Hejtmanek, Phase equilibria in Ca-Co-O system, *J. Solid State Chem.* 194 (2012) 199–205.

38. D. Kenfaui, D. Chateigner, M. Gomina, J. G. Noudem, Texture, mechanical and thermoelectric properties of $Ca_3Co_4O_9$ ceramics, *J. Alloys Compds.* 490 (2010) 472–479.

39. M. Bittner, L. Helmich, F. Nietschke, B. Geppert, O. Oeckler, A. Feldhoff, Porous $Ca_3Co_4O_9$ with enhanced thermoelectric properties derived from Sol–Gel synthesis, *J. Eur. Ceram. Soc.* 37 (2017) 3909–3915.

40. T. Schulz, J. Topfer, Thermoelectric properties of $Ca_3Co_4O_9$ ceramics prepared by an alternative pressure-less sintering/annealing method, *J. Alloys Compds.* 659 (2016) 122–126.

41. M. A. Madre, F. M. Costa, N. M. Ferreira, A. Sotelo, M. A. Torres, G. Constantinescu, Sh. Rasekh, J. C. Diez, Preparation of high-performance $Ca_3Co_4O_9$ thermoelectric ceramics produced by a new two-step method, *J. Eur. Ceram. Soc.* 33 (2013) 1747–1754.

42. F. Delorme, D. Ovono Ovono, P. Marudhachalam, C. Fernandez Martin, O. Fraboulet, Effect of precursors size on the thermoelectric properties of $Ca_3Co_4O_9$ ceramics, *Mater. Res. Bull.* 47 (2012) 1169–1175.

43. L. Daheron, R. Dedryvere, H. Martinez, M. Menetrier, C. Denage, C. Delmas, D. Gonbeau, Electron transfer mechanisms upon lithium deintercalation from $LiCoO_2$ to CoO_2 investigated by XPS, *Chem. Mater.* 20 (2008) 583–590.

44. Y. Wakisaka, S. Hirata, T. Mizokawa, Y Suzuki, Y. Miyazaki, T. Kajitani, Electronic structure of $Ca_3Co_4O_9$ studied by photoemission spectroscopy: Phase separation and charge localization, *Phys. Rev. B* 78 (2008) 235107.

45. J.-C. Dupin, D. Gonbeau, P. Vinatier, A. Levasseur, Systematic XPS studies of metal oxides, hydroxides and peroxides, *Phys. Chem. Chem. Phys.* 2 (2000) 1319–1324.

46. M. I. Sosulnikov, Y. A. Teterin, X-Ray photoelectron studies of Ca, Sr and Ba and their oxides and carbonates, *J. Electron. Spectrosc. Relat. Phenom.* 59 (1992) 111–126.

47. A. B. Christie, J. Lee, I. Sutherland, J. M. Walls, An XPS study of ion-induced compositional changes with group-II and group-IV compounds, *Appl. Surf. Sci.* 15 (1983) 224–237.

48. R. L. Frost, M. C. Hales, W. N. Martens, Thermogravimetric analysis of selected group (II) carbonate minerals – implication for the geosequestration of greenhouse gas, *J. Therm. Anal. Calorim.* 95 (2009) 999–1005.

49. M. A. Madre, F. M. Costa, N. M. Ferreira, S. I. R. Costa, Sh. Rasekh, M. A. Torres, J. C. Diez, V. S. Amaral, J. S. Amaral, A. Sotelo, High thermoelectric performance in

$Bi_{2-x}Pb_xBa_2Co_2O_y$ promoted by directional growth and annealing, *J. Eur. Ceram. Soc.* 36 (2016) 67–74.

50. N. Y. Wu, T. C. Holgate, N. V. Nong, N. Pryds, S. Linderoth, High temperature thermoelectric properties of $Ca_3Co_4O_{9+\delta}$ by auto-combustion synthesis and spark plasma sintering, *J. Eur. Ceram. Soc.* 34 (2014) 925–931.

51. J. G. Noudem, D. Kenfaui, D. Chateigner, M. Gomina, Toward the enhancement of thermoelectric properties of lamellar $Ca_3Co_4O_9$ by edge-free spark plasma texturing, *Scr. Mater.* 66 (2012) 258–260.

52. W. Koshibae, K. Tsuitsui, S. Maekawa, Thermopower in cobalt oxides, *Phys. Rev. B Condens. Matter* 62 (2000) 6869–6872.

53. A. Maignan, D. Pelloquin, S. Hebert, Y. Klein, M. Hervieu, Thermoelectric Power In Misfit Cobaltites Ceramics: Optimization By Chemical Substitutions, *Bol. Soc. Esp. Ceram. V.* 45 (2006) 122–125.

54. M. Karppinen, H. Fjellvag, T. Konno, Y. Morita, T. Motohashi, H. Yamauchi, Evidence for Oxygen Vacancies in Misfit-Layered Calcium Cobalt Oxide, $[CoCa_2O_3]_qCoO_2$, *Chem. Mater.* 16 (2004) 2790–2793.

55. A. Sotelo, G. Constantinescu, Sh. Rasekh, M. A. Torres, J. C. Diez, M. A. Madre, Improvement of thermoelectric properties of $Ca_3Co_4O_9$ using soft chemistry synthetic methods, *J. Eur. Ceram. Soc.* 32 (2012) 2415–2422.

56. Sh. Rasekh, M. A. Torres, G. Constantinescu, M. A. Madre, J. C. Diez, A. Sotelo, Effect of Cu by Co substitution on $Ca_3Co_4O_9$ thermoelectric ceramics, *J. Mater. Sci. Mater. Electron.* 24 (2013) 2309–2314.

57. H. Yamauchi, L. Karvonen, T. Egashira, Y. Tanaka, M. Karppinen, Ca-for-Sr substitution in the thermoelectric $[(Sr,Ca)_2(O,OH)_2]_q[CoO_2]$ misfit-layered cobalt-oxide system, *J. Solid State Chem.* 184 (2011) 64–69.

58. K. Saito, R. Okazaki, Electron correlation effect in the thermoelectric oxide $Ca_{3-x}Sr_xCo_4O_9$ single crystals, *Jpn. J. Appl. Phys.* 56 (2017) 043201.

59. S. Fujii, M. Yoshiya, Manipulating thermal conductivity by interfacial modification of misfit-layered cobaltites $Ca_3Co_4O_9$, *J. Electron. Mater.* 45 (2016) 1217–1226.

60. A. Sotelo, F. M. Costa, N. M. Ferreira, A. Kovalevsky, M. C. Ferro, V. S. Amaral, J. S. Amaral, Sh. Rasekh, M. A. Torres, M. A. Madre, J. C. Diez, Tailoring $Ca_3Co_4O_9$ microstructure and performances using a transient liquid phase sintering additive, *J. Eur. Ceram. Soc.* 36 (2016) 1025–1032.

Figure captions

Figure 1. Powder XRD patterns of undoped and Sr-doped $Ca_3Co_4O_9$ samples. Diffraction planes indicate the reflections corresponding to $Ca_3Co_4O_9$ phase, while * identify those associated to $Ca_3Co_2O_6$ one.

Figure 2. Representative SEM micrographs taken on a) fractured transversal sections of $Ca_3Co_4O_9$ samples (The arrow indicates the pressure direction in the cold and the hot uniaxial pressing processes); and b) polished surface of Sr-doped samples after chemical etching.

Figure 3: XPS spectra obtained in undoped (-); and Sr-doped (-) $Ca_3Co_4O_9$ samples, for a) Co 2p; b) Ca 2p; and c) Sr 3d spectra in Sr-doped ones.

Figure 4: Auger analyses of two target dots in the undoped material: (a) SEM image with the location of the two dots and (b) the corresponding Auger spectra.

Figure 5: Auger analyses of two target dots for the Sr-doped material: (a) SEM image showing a Sr-inclusion and the location of the two target dots and (b) the corresponding Auger spectra.

Figure 6: a) Temperature dependence of the electrical resistivity (filled symbols) and Seebeck coefficient (empty symbols) for the undoped (●, ○); and Sr-doped (■, □) $Ca_3Co_4O_9$ samples, together with their errors; b) Temperature dependence of the power factor for the undoped (●); and Sr-doped (■) $Ca_3Co_4O_9$ samples, together with their error.

Figure 7: a)Temperature dependence of thermal conductivity for undoped (●); and Sr-doped (■) samples, together with their errors; and b) Temperature dependence of ZT for undoped (●); and Sr-doped (■) samples, together with their error. The vertical line is

a guide for eyes to separate the calculated (low temperatures) and estimated values (high temperatures), considering thermal conductivity constant in the whole temperature range.